J. Fluid Mech. (2026), *vol.* 1037, A52, doi:10.1017/jfm.2026.11594

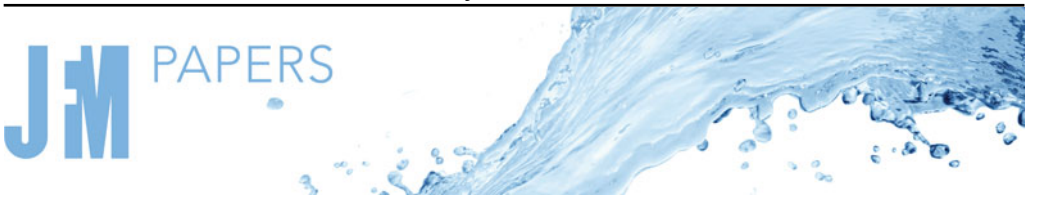

Prediction of bypass transition from wall measurements

Dandan Xiao[1], **Jan Oscar Pralits**[2] **and Xuerui Mao**[3,4]

[1]School of Aerospace Engineering, Beijing Institute of Technology, Beijing 100081, PR China

[2]DICCA, University of Genova, Via Montallegro 1, Genova 16145, Italy

[3]Beijing Institute of Technology (Zhuhai), Zhuhai, PR China

[4]State Key Laboratory of Explosion Science and Safety Protection, Beijing 100081, PR China

Corresponding author: Xuerui Mao, maoxuerui@sina.com

(Received 15 December 2024 UTC; revised 26 February 2026 UTC; accepted 19 April 2026 UTC)

Prediction of bypass transition from wall measurements in a zero-pressure-gradient boundary-layer flow over a flat plate with a leading edge is investigated using adjoint-variational optimisation techniques and Hessian analyses. The reference wall data are obtained from separate direct numerical simulations subjected to inflows with increasing levels of complexity. The prediction is achieved by reconstructing an inflow profile that generates wall data matching the reference. Initially, the algorithm is validated through steady inflows constructed from a single vortical mode. Positive streaks are reconstructed accurately, while negative streak predictions worsen with increasing turbulence intensity due to their reduced wall impact. Hessian analysis reveals that, under low turbulence intensity, the most observable inflow structures deviating from the optimal profile align with classical streak-generating modes, whereas at higher turbulence levels, the dominant observable directions shift toward spanwise uniform perturbations in high-shear regions, highlighting a reduced estimation robustness. Secondly, an inflow constructed from multiple vortical modes effectively demonstrates the prediction of streak meandering motions, with the optimised inflow profile differing significantly from the reference one. Finally, a more elaborate inflow in the form of free-stream turbulence is used to trigger bypass transition, and the results indicate that primary flow structures can be reconstructed, while the accuracy of the details improves when more downstream measurement data are included. These findings highlight the potential for accurate reconstruction of boundary-layer transition from wall measurement data.

Key words: boundary layers, transition to turbulence

1. Introduction

Laminar-to-turbulence transition has been a long-lasting challenge for the fluid mechanics community due to its high sensitivity to environmental uncertainties. Even a small change in the spectral makeup of the free-stream conditions can lead to qualitative changes in the transition mechanism and quantitative changes in its location. Measurements, or observations, can help reduce these uncertainties (Zaki 2025); however, in realistic configurations, flow data are often only available at the wall. In this work, we attempt to predict the inflow conditions that result in the available wall measurements under the scenario of bypass transition. The results demonstrate how the chaotic nature of transition complicates this task and serve as a benchmark for other algorithms addressing this challenge.

The boundary-layer flow is known to amplify environmental disturbances, generating large coherent structures whose breakdown leads to transition to turbulence. When this process involves discrete instability waves at supercritical Reynolds numbers, it is termed orderly or natural transition. However, in the presence of finite-amplitude environmental perturbations, especially broadband free-stream turbulence (FST), another form of transition process, termed bypass transition, takes place (Zaki 2013). The boundary layer filters the free-stream spectrum and only low-frequency disturbances are amplified by the mean shear. These disturbances subsequently undergo secondary instabilities, which give way to sporadic bursts of turbulent spots. The spots, which spread as they advect downstream, already exhibit a fully turbulent dynamics within their core (Nolan & Zaki 2013; Marxen & Zaki 2019) and a fractal geometry at the interface that separates them from the outside laminar flow (Wu *et al.* 2020). Bypass transition is therefore chaotic in its onset and evolution, and its detailed description is sensitive to the environmental conditions, making it inherently challenging to compute flow sensitivity for applications like optimal control, optimal perturbation analyses and estimation of flow conditions.

Techniques for estimating instantaneous flow states or predicting the evolution of flow variables can be generally classified as data driven and model based. The data-driven method seeks the relationship between the measurements, i.e. input, and the flow state, i.e. output, without any prior knowledge of the mathematical equations governing the flow. Linear stochastic estimation, which utilises second-order correlations between the measured data and the variable to be predicted, is one of the data-driven techniques and has been used to estimate wall-bounded turbulent flow (Adrian & Moin 1988; Suzuki & Hasegawa 2017; Liu & Hasegawa 2020). Additionally, owing to the rapid development of computer hardware and numerical algorithms in the past decade, artificial neural networks (ANNs) have demonstrated growing success in predicting turbulence (Milano & Koumoutsakos 2002; Fukami *et al.* 2019; Du *et al.* 2023). By learning complex patterns and features from large datasets, ANN models can capture the intricate dynamics of turbulent flows that traditional methods may miss (Duraisamy *et al.* 2019).

In contrast to data-driven approaches, which usually require massive data, the model-based method is built on the governing equations that describe flow systems. Among these approaches, resolvent-based estimation has emerged as a promising framework for reconstructing unmeasured flow quantities from limited observations. Building on the resolvent framework of McKeon & Sharma (2010), in which the Navier–Stokes equations linearised around the mean are driven by the nonlinear terms considered as a forcing, Towne *et al.* (2020) introduced a statistical resolvent-based method that infers the cross-spectral density of the nonlinear forcing from limited data and, via the resolvent operator, estimates the corresponding space–time flow statistics without a rank-1 assumption. Subsequently, Martini *et al.* (2020) extended the approach to an optimal estimator for time-varying flow fields in transitional and turbulent regimes. Their method, based on a

matrix-free implementation of direct and adjoint linearised operators, enables accurate estimation without relying on *a priori* model reduction. More recently, Amaral *et al.* (2021) applied the resolvent-based method to turbulent channel flow and showed that structures leaving measurable footprints can be accurately estimated from wall shear stress and pressure data across a wide Reynolds number range.

A key advantage of resolvent-based approaches lies in their incorporation of prior physical knowledge through linearised operators, which act as a regularising mechanism and enhance estimation robustness, particularly under sparse observational conditions. In contrast, other model-based estimation methods, such as those extensively developed and widely applied in the meteorological community, primarily rely on observational data to constrain model evolution (Rabier 2005; Kalnay *et al.* 2007). These approaches are typically Bayesian-based and include traditional variation data assimilation (Talagrand & Courtier 1987; Rawlins *et al.* 2007), ensemble-based Kalman filters (Houtekamer & Zhang 2016) and Monte Carlo techniques. While the variational and ensemble methods are widely used in numerical weather prediction, each possesses inherent limitations (Bannister 2017), which has motivated the development of hybrid techniques that seek to combine their respective strengths while mitigating individual shortcomings (Zhang *et al.* 2009).

Inspired by similar principles, model-based estimation in fluid mechanics can also be categorised according to how measurements are assimilated: filtering methods update the flow state sequentially using the most recent data, whereas smoothing methods seek a state trajectory that best fits observations over an entire time window (Wang & Zaki 2021). Hœpffner *et al.* (2005) used the Kalman filter, a typical filter approach, to estimate perturbations in laminar flows. To account for nonlinearity, Chevalier *et al.* (2006) and Colburn *et al.* (2011) applied the extended Kalman filter and ensemble Kalman filter, respectively, to estimate turbulent channel flow from wall measurements. However, as mentioned before, since the filtering approach attempts to match the measurement at the last moment rather than over the entire interval, its accuracy is limited (Zaki & Wang 2021).

In contrast, the smoothing approaches seek to estimate the entire flow state over a finite time window, such that the predicted evolution of the nonlinear system optimally matches the available measurements throughout the interval (Bewley & Protas 2004). It typically uses iterative looping over the forward and adjoint equations, where the optimal initial conditions, boundary conditions or model parameters are obtained by defining a cost function that measures the differences between the estimation and target data. Adjoint techniques have shown success in finding optimal boundary conditions in transitional flow (Mao *et al.* 2013, 2017), suppressing transitional flow (Xiao & Papadakis 2017) and estimating scalar sources from remote measurements in turbulent flow (Wang *et al.* 2019*b*). More recently, Wang & Zaki (2021) applied an adjoint-variational approach to estimate the initial condition of turbulent channel flow from limited measurements of velocity data.

While many of the aforementioned estimation strategies have demonstrated success in channel flows, their extension to boundary-layer flows has been less explored. Here, we consider a spatially developing transitional boundary layer and perform wall-based estimation using an adjoint-variational framework. As noted by Bewley *et al.* (2001), one of the earliest applications of adjoint-based optimisation to turbulent flows, the framework is computationally intensive and therefore currently restricted to offline implementation; nevertheless, it provides an optimal benchmark, i.e. the best achievable performance permitted by the governing dynamics and the available observations. The present study aims to explore the theoretical limits of reconstructing boundary-layer flows from an observer's perspective and to quantify flow observability (Zaki 2025).

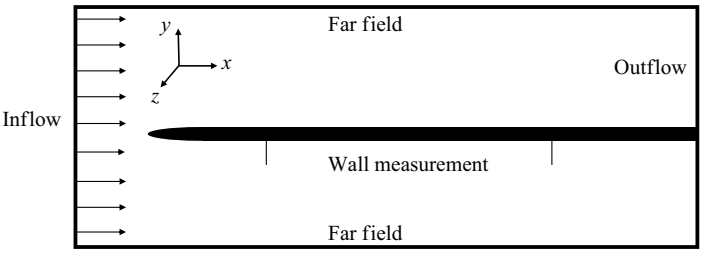

Figure 1. Schematic diagram of the flow configuration and the coordinate system. The leading edge is located at the origin.

The rest of the paper is organised as follows. In § 2, the adjoint-variational method, formulation of the Hessian matrix and the computational set-up are introduced. The proposed methods are first examined through the prediction of streaks induced by simple steady inflow with various turbulence intensities in § 3. In § 4, a more complex inflow profile with multiple vortical modes is constructed to demonstrate the prediction of streak meandering motions. Finally in § 5, the prediction of bypass transition triggered by full-spectrum FST is performed with discussions on the performance, sensitivity to inflow conditions, effect of optimisation time and Hessian analysis. In § 6 the main observations are summarised.

2. Theoretical formulation and computational set-up

2.1. *Governing equations*

The flow configuration of interest is a boundary layer developing over a flat plate with a slender elliptic leading edge, as shown in figure 1, which has been adopted in several previous studies (Mao *et al.* 2013, 2015; Wang *et al.* 2019*a*). The leading edge is located at the origin and has an aspect ratio of $AR = 20$. The flow is governed by the incompressible Navier–Stokes (NS) equations,

$$\partial_t \boldsymbol{u} + \boldsymbol{u} \cdot \boldsymbol{\nabla} \boldsymbol{u} + \boldsymbol{\nabla} p - Re^{-1} \boldsymbol{\nabla}^2 \boldsymbol{u} = 0, \quad \boldsymbol{\nabla} \cdot \boldsymbol{u} = 0, \tag{2.1}$$

where $\boldsymbol{u} = (u, v, w)^{\mathrm{T}}$ and p represent the non-dimensional velocity and pressure with u, v and w being the streamwise, wall-normal and spanwise velocity components, respectively. The Reynolds number $Re = U_\infty R/\nu$ is based on the free-stream velocity U_∞, the kinematic viscosity ν and a reference length R, which is the half-thickness of the flat plate. For analyses, the flow variables in (2.1) are decomposed as

$$(\boldsymbol{u}, p) = (\boldsymbol{U}, P) + \left(\boldsymbol{u}', p'\right), \tag{2.2}$$

where $(\boldsymbol{U}, P)$ with $\boldsymbol{U} = (U, V, 0)^{\mathrm{T}}$ is the two-dimensional (2-D) and steady solution of (2.1) and $(\boldsymbol{u}', p')$ with $\boldsymbol{u}' = (u', v', w')^{\mathrm{T}}$ is the perturbation. As bypass transition is convective and is triggered by the inflow disturbance, consider a flow starting from a 2-D steady solution of (2.1) and perturbed by an inflow condition in the form

$$\boldsymbol{u}(\boldsymbol{x}_{in}, t) = U_\infty + G(t)\boldsymbol{u}_{in}, \tag{2.3}$$

where $\boldsymbol{x}_{in}$ denotes the spatial coordinates on the inflow boundary. The parameter $G(t)$ is given by

$$G(t) = \left(1 - e^{-\sigma t^2}\right)\left(1 - e^{-\sigma (T-t)^2}\right), \tag{2.4}$$

where σ is a relaxation factor and is set to $\sigma = 100$ throughout this work and T is the total optimisation time. Here, $G(t)$ is used to force the inflow $\boldsymbol{u}_{in}$ at $t = 0$ and $t = T$ to be zero, which eliminates spatial and temporal discontinuities that would otherwise arise during the forward and adjoint simulations. This formulation has been elaborated in Mao *et al.* (2013) and applied in several other scenarios (Mao *et al.* 2015; Wang *et al.* 2019*a*).

2.2. *Adjoint-variational optimisation*

Owing to the convective nature of the flow scenario considered, the prediction of bypass transition can be realised through the prediction of the inflow profile, which leads to the same flow development as the reference one. The prediction is then transformed into an adjoint-based optimisation problem with an objective function defined based on the streamwise velocity gradient at the wall

$$J = \int_0^T \int_{S_W} \left(\frac{\partial u}{\partial y} - \frac{\partial u_r}{\partial y} \right)^2 \mathrm{d}S_W \mathrm{d}t, \tag{2.5}$$

where S_W denotes the part of the wall where data measurement is collected and the subscript r denotes the reference variable. The streamwise velocity gradient is used in the objective function because pre-transitional flows are predominantly characterised by streamwise velocity fluctuations caused by the presence of velocity streaks (Matsubara & Alfredsson 2001).

A Lagrangian $\mathcal{L}$ is defined with the aim of obtaining the inflow perturbation $\boldsymbol{u}'_{in}(\boldsymbol{x}_{in}, t)$ that minimises the objective function (2.5), while satisfying the governing (2.1)

$$\mathcal{L} = J - \int_0^T \int_{\Omega} \left[\boldsymbol{u}^\dagger \cdot \left(\partial_t \boldsymbol{u} + \boldsymbol{u} \cdot \nabla \boldsymbol{u} + \nabla p - Re^{-1} \nabla^2 \boldsymbol{u} \right) + p^\dagger \cdot (\nabla \cdot \boldsymbol{u}) \right] \mathrm{d}\Omega \mathrm{d}t, \tag{2.6}$$

where $\boldsymbol{u}^\dagger$ and $p^\dagger$ are the adjoint velocity field and pressure, respectively.

A differentiate-then-discretise approach is used. At the stationary point, the first-order variation of the Lagrangian with respect to each variable is required to vanish. Setting the variation with respect to the adjoint variables to zero recovers the governing (2.1). Setting the variation of $\mathcal{L}$ with respect to $(\boldsymbol{u}, p)$ to zero and after integration by parts, a set of linear adjoint equations is derived

$$-\partial_t \boldsymbol{u}^\dagger - \boldsymbol{u} \cdot \nabla \boldsymbol{u}^\dagger + \nabla \boldsymbol{u} \cdot \boldsymbol{u}^\dagger - \nabla p^\dagger - Re^{-1} \nabla^2 \boldsymbol{u}^\dagger = 0, \quad \nabla \cdot \boldsymbol{u}^\dagger = 0, \tag{2.7}$$

which equations are integrated backwards in time from $t = T$ to $t = 0$. A more detailed derivation of the adjoint equations can be found in Barkley *et al.* (2008). The terminal and boundary conditions for the adjoint variables are determined during the derivation of the adjoint equations where the integration over all the boundaries and time must be zero. The terminal condition for the adjoint variable is $\boldsymbol{u}^\dagger(T) = 0$ since the disturbance is only introduced from the boundary (Mao *et al.* 2013). On the inflow, wall (no measurement) and far-field boundaries, zero Dirichlet and Neumann conditions are used for $\boldsymbol{u}^\dagger$ and $p^\dagger$, respectively. A convective outflow boundary condition is adopted at the outlet (Mao *et al.* 2013). The boundary condition for $\boldsymbol{u}^\dagger$ on the wall where measurements are collected is

$$u^\dagger = 2Re \left(\frac{\partial u}{\partial y} - \frac{\partial u_r}{\partial y} \right), \quad v^\dagger = w^\dagger = 0. \tag{2.8}$$

Finally, the variation of $\mathcal{L}$ with respect to the inflow gives the gradient, i.e. the first-order derivative denoted as $\boldsymbol{g}$

$$\boldsymbol{g} = p^\dagger \boldsymbol{n} - Re^{-1} \nabla_{\boldsymbol{n}} \boldsymbol{u}^\dagger, \tag{2.9}$$

where $\boldsymbol{n}$ is the unit vector pointing outwards of the inflow boundary, and $\nabla_{\boldsymbol{n}}$ denotes the normal derivative. This gradient is used to update the inflow at the end of each iteration

$$\boldsymbol{u}_{in}^{k+1} = \boldsymbol{u}_{in}^{k} - \alpha \boldsymbol{g}, \tag{2.10}$$

where k is the iteration step and α is the optimal step length, determined at each iteration by minimising the objective function along the descent direction to ensure smooth and efficient convergence. A more detailed mathematical derivation can be found in Mao *et al.* (2013).

Equations (2.1) and (2.7) form a forward–backward loop that is solved iteratively over an optimisation time period T. The optimisation procedure to predict bypass transition is summarised below.

(i) Reference case
  (*a*) Solve the NS (2.1) from $t = 0$ to $t = T$ with a reference inflow disturbance and a 2-D steady solution as the initial condition, and store the wall measurement at every time step.

(ii) Adjoint optimisation
  (*a*) Select an initial guess for the inflow.
  (*b*) March the forward (2.1) from $t = 0$ to $t = T$.
  (*c*) At $t = T$, evaluate the objective function (2.5): the iteration loop stops if convergence is achieved, otherwise it continues to step (*d*).
  (*d*) Integrate the adjoint (2.7) backwards from $t = T$ to $t = 0$.
  (*e*) Compute the gradient of the cost function (2.9).
  (*f*) Update the inflow using (2.10) and repeat the procedure from step (*b*).

(iii) Prediction case
  (*a*) Solve (2.1) with the predicted inflow from the adjoint optimisation and compare the flow development with the reference case.

The optimisation procedure requires iterative integration of the NS (2.1) and the adjoint (2.7). In addition, because the adjoint (2.7) depend explicitly on the forward flow fields, these fields must be stored during the forward simulation at every time step and reloaded during the backward integration. For the largest cases considered in this study, the computational cost is more than 50 000 CPU hours, with a storage requirement of approximately 50 TB.

2.3. *Hessian matrix*

The Hessian matrix represents the second-order partial derivatives of a scalar function. It is widely used in large-scale optimisation problems as it determines the rate of convergence of descent algorithms for minimising a cost function (Thacker 1989). In this work, Hessian analysis is performed and the eigenvalue/eigenvectors are used to further explore the numerical effectiveness of using the wall measurement data to reconstruct the inflow. However, computing the full Hessian matrix directly is often impractical in high-dimensional systems due to the prohibitive cost of storage and computation. Following Wang *et al.*'s (2022) work on the initial condition problem, an alternative variational state-estimation approach, which allows efficient construction of Hessian by examining small perturbations around the optimal solution, is adopted. Before continuing the derivation of the Hessian, we first introduce two scalar products defined on the entire computational

domain Ω and the inflow boundary S_{in}

$$(\boldsymbol{a}, \boldsymbol{b}) = \int_{\Omega} \boldsymbol{a} \cdot \boldsymbol{b} \mathrm{d}\Omega, \quad [\boldsymbol{c}, \boldsymbol{d}] = \int_0^T \int_{S_{in}} \boldsymbol{c} \cdot \boldsymbol{d} \mathrm{d}S_{in}\mathrm{d}t, \tag{2.11}$$

where $\boldsymbol{a}$, $\boldsymbol{b}$ and $\boldsymbol{c}$, $\boldsymbol{d}$ are vectors defined within Ω and S_{in}, respectively.

The deviations between the reference field $(\boldsymbol{u}_r, p_r)$ and the predicted one $(\boldsymbol{u}, p)$ are defined as $(\tilde{\boldsymbol{u}}, \tilde{p}) = (\boldsymbol{u}_r, p_r) - (\boldsymbol{u}, p)$. When the prediction is close enough to the reference field, the deviation can be governed by the linearised NS equations

$$\partial_t \tilde{\boldsymbol{u}} + \boldsymbol{u} \cdot \nabla \tilde{\boldsymbol{u}} + \nabla \boldsymbol{u} \cdot \tilde{\boldsymbol{u}} + \nabla \tilde{p} - Re^{-1} \nabla^2 \tilde{\boldsymbol{u}} = 0, \quad \nabla \cdot \tilde{\boldsymbol{u}} = 0. \tag{2.12}$$

The corresponding inflow condition for the linearised (2.12) is $\tilde{\boldsymbol{u}}_{in} = \boldsymbol{u}_{in,r} - \boldsymbol{u}_{in}$.

To evaluate the local observability of wall measurements with respect to inflow perturbations, we define a localised cost functional at the final time T and a specific wall location $\boldsymbol{x}_m$, covering an area of S_m, given by

$$J_m = \int_{S_m} \left(\frac{\partial \tilde{u}}{\partial y} \right)^2 \mathrm{d}S_m. \tag{2.13}$$

This formulation isolates the contribution of wall shear mismatch over a localised location, enabling the construction of a Hessian matrix that quantifies the influence of inflow perturbations on the local wall response.

Note that, at the true solution $\tilde{\boldsymbol{u}} = \boldsymbol{u}_r - \boldsymbol{u} = 0$, the gradient of J_m with respect to the deviated inflow $\tilde{\boldsymbol{u}}_{in}$ vanishes. The Hessian matrix for J_m, defined as the second-order derivative of J_m with respect to the inflow $\boldsymbol{u}_{in}$, can be obtained by solving (2.12) using the inflow condition $\tilde{\boldsymbol{u}}_{in}$. However, for the steady case, such an approach requires $O(3 \times N_y \times N_z)$ simulations (N_y and N_z are the number of grid points in the wall-normal and spanwise directions, respectively) as each possible spatial location in the inflow boundary plane must be perturbed for all three velocity components. This can be avoided by utilising the duality relation of (2.12) and the corresponding adjoint equations (Mao *et al.* 2013). The impact of a deviation $\tilde{\boldsymbol{u}}$ at $t = T$ and $\boldsymbol{x}_m$ can be expressed as

$$\int_{S_m} \left(\frac{\partial \tilde{u}}{\partial y} \right) \mathrm{d}S_m = (\boldsymbol{\phi}, \tilde{\boldsymbol{u}}), \tag{2.14}$$

where $\boldsymbol{\phi}$ represents a unit wall-normal derivative kernel centred at $\boldsymbol{x}_m$, defined over a unit wall-normal distance from the wall and zero elsewhere. This reformulation allows the Hessian to be evaluated by perturbing wall locations instead of all inflow degrees of freedom.

Then the duality relation is

$$(\tilde{\boldsymbol{u}}, \boldsymbol{\phi}) = (\mathcal{A}\tilde{\boldsymbol{u}}_{in}, \boldsymbol{\phi}) = \left[\tilde{\boldsymbol{u}}_{in}, \mathcal{A}^{\dagger}\boldsymbol{\phi} \right] = \left[\tilde{\boldsymbol{u}}_{in}, \tilde{\boldsymbol{g}} \right]. \tag{2.15}$$

In the first equality in (2.15), $\tilde{\boldsymbol{u}}$ is expressed by $\mathcal{A}\tilde{\boldsymbol{u}}_{in}$, where $\mathcal{A}$ denotes the linear operator associated with the forward integration of (2.12). Following the variational formulation, a set of adjoint equations of (2.12) can be obtained and their integration can be represented as $\mathcal{A}^{\dagger}$, the adjoint of $\mathcal{A}$. The second equality in (2.15) arises from the standard duality pairing between the forward and adjoint systems (Mao *et al.* 2013), where $\boldsymbol{\phi}$ is propagated backward by the adjoint operator $\mathcal{A}^{\dagger}$. In the last term in (2.15), $\tilde{\boldsymbol{g}}$ is the corresponding gradient with respect to the inflow deviation, expressed in the form given by (2.9).

Now the objective function (2.13) can be rewritten using the duality relation (2.15)

$$J_m = (\tilde{\boldsymbol{u}}, \boldsymbol{\phi})^2 = \left[\tilde{\boldsymbol{u}}_{in}, \tilde{\boldsymbol{g}} \right]^2, \tag{2.16}$$

Mesh nos.	§	x span	y span	z span	Wall measurement in x	T	n_e	n_z
1	3.1	$[-20, 60]$	$[-40, 40]$	$[0, 7.2]$	$[20, 60]$	100	1341	48
2	3.2	$[-20, 100]$	$[-40, 40]$	$[0, 20]$	$[10, 90]$	150	1924	144
3	3.3	$[-20, 200]$	$[-40, 40]$	$[0, 20]$	$[10, 140]$	200	2971	144

Table 1. Parameters of the computation. Here, T is the optimisation time, n_e is the number of elements in each $x-y$ plane and n_z is the number of Fourier modes in the spanwise direction. The measurement region covers the full spanwise domain.

by assuming S_m has a unit value without loss of generality. Then the Hessian matrix is obtained as

$$\mathcal{H} = \frac{\partial^2 J_m}{\partial \tilde{\boldsymbol{u}}_{in} \partial \tilde{\boldsymbol{u}}_{in}} = 2\tilde{\boldsymbol{g}}\tilde{\boldsymbol{g}}^T. \tag{2.17}$$

The Hessian matrix characterises how sensitive the cost function (2.13) is to small perturbations in the inflow near the optimal solution. Its eigenvectors indicate the principal directions along which changes in the inflow influence the wall measurements at the specified location, while the corresponding eigenvalues reflect the strength of that influence. A large eigenvalue suggests that a small inflow perturbation in that direction leads to a significant increase in the cost, meaning that such directions are more observable and can be more efficiently corrected during gradient-based optimisation. Conversely, directions associated with small eigenvalues have a weaker impact on the cost and tend to converge more slowly.

Note that the Hessian matrix constructed from (2.17) has a size of $(3N_yN_z)^2$, which is time consuming to compute and to perform eigenvalue analyses on. Since the forward flow is homogeneous in the spanwise direction, the eigenvectors of the Hessian in the spanwise direction are Fourier modes (Wang *et al.* 2022). Therefore a Fourier transform is first performed on the gradient field $\tilde{\boldsymbol{g}}$, and the Hessian for each spanwise wavenumber β can be expressed as

$$\hat{\mathcal{H}}_z(\beta) = 2\mathcal{F}(\tilde{\boldsymbol{g}})\mathcal{F}^*(\tilde{\boldsymbol{g}}), \tag{2.18}$$

where $\mathcal{F}(\tilde{\boldsymbol{g}})$ represents the Fourier transform of $\tilde{\boldsymbol{g}}$ in the z direction and $\mathcal{F}^*(\tilde{\boldsymbol{g}})$ denotes the corresponding complex conjugate.

2.4. *Computational parameters*

A spectral element method is adopted to discretise the NS (2.1) and the adjoint (2.7) in the $x-y$ plane (Karniadakis & Sherwin 2005). Each $x-y$ plane consists of n_e elements (table 1), clustered around the upper side of the flat plate. Each element is further decomposed into a $(\mathcal{P}+1) \times (\mathcal{P}+1)$ grid, where $\mathcal{P}$ is the polynomial order that defines the resolution. In this work, $\mathcal{P} = 6$ is adopted for all three meshes after convergence tests. In the spanwise direction, the flow variables are decomposed into n_z Fourier modes. Since the forward–backward simulation requires a significant amount of computational cost and storage, three domains with different sizes, resolutions and wall measurement regions are adopted for cases with different inflow conditions and optimisation times, as listed in table 1.

The 2-D base flow is obtained by solving the full nonlinear NS (2.1) until a steady state is achieved. Figure 2 shows the 2-D steady flow profile over the upper part of the flat plate using mesh 3 in table 1 as an example. The boundary-layer thickness reaches approximately $y = 2.9$ at the outlet $x = 200$. The Reynolds number $Re = 800$ is adopted

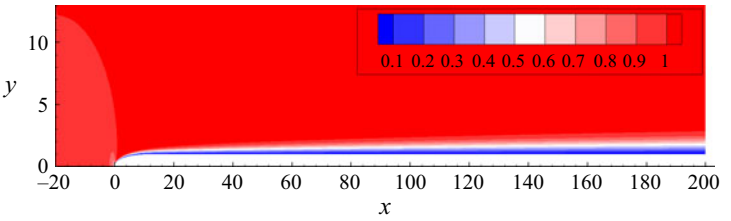

Figure 2. Contour of streamwise velocity of the 2-D steady flow around the upper part of the flat plate at $Re = 800$.

throughout this work. As can be seen from figure 1, a zero-pressure-gradient boundary layer develops downstream of the leading edge. Further validation of the simulation can be found in Wang *et al.* (2019*a*).

3. Prediction of streaks

In this section, we apply the optimisation procedure to predict streamwise velocity streaks induced by a steady vortical inflow disturbance. This scenario not only enables straightforward validation of the algorithm, but also provides a unique interpretation of the optimisation and Hessian analysis results. The inflow perturbation is constructed using Fourier modes of the form

$$\boldsymbol{u}_{in} = \boldsymbol{U}_{in} + \epsilon \sum \hat{\boldsymbol{u}}_{in} e^{i(\gamma_{in} y + \beta_{in} z)}, \tag{3.1}$$

where γ_{in} and β_{in} are wall-normal and spanwise wavenumbers, respectively, ϵ is a constant that determines the magnitude of the inflow disturbance and $\boldsymbol{U}_{in} = (U_\infty, 0, 0)^{\mathrm{T}}$. Considering an inflow disturbance in the form of streamwise vorticity only and applying the continuity equation, the amplitude $\hat{\boldsymbol{u}}_{in}$ at a given γ_{in}, β_{in} is (Schrader *et al.* 2010)

$$\hat{\boldsymbol{u}}_{in} = (\hat{u}_{in}, \hat{v}_{in}, \hat{w}_{in})^{\mathrm{T}} = \frac{i}{\sqrt{\gamma_{in}^2 + \beta_{in}^2}} (0, \beta_{in}, -\gamma_{in})^{\mathrm{T}}. \tag{3.2}$$

We start with the inflow consisting of only one steady vortical mode with parameters $(\gamma_{in}, \beta_{in}) = (2.618, 1.85)$. Four levels of turbulence intensity ($Tu = 0.01$ %, 0.1 %, 1 % and 3 %) of the inflow disturbance are considered to demonstrate the robustness of the algorithm. Mesh 1 in table 1 is used for all simulations in this section. The optimisation time T is set to 100, ensuring that the inflow is convected beyond the end of the wall measurement region, i.e. $x = 60$. The initial guesses of the inflow, i.e. the initial condition of the optimisation, for all cases are set to zero.

Figure 3 illustrates the effectiveness of the optimisation algorithm in achieving rapid convergence for different turbulence intensity levels. The cost function is normalised by its value at the start of the iteration. The dramatic initial decreases in J highlight the adopted algorithm's efficiency in updating the inflow conditions to closely match the reference flow within a few iterations. The rapid convergence is particularly notable at lower turbulence intensities, where the algorithm's performance is most effective. Further reducing the turbulence intensity (from $Tu = 0.1$ % to $Tu = 0.01$ %) does not improve convergence, indicating a threshold has been reached in the linear region. As the turbulence intensity increases, the reduction in J becomes more challenging, reflecting the increased complexity and nonlinearity of the flow. This is evident from the higher values of $J/J(0)$ at $Tu = 1$ % and $Tu = 3$ %.

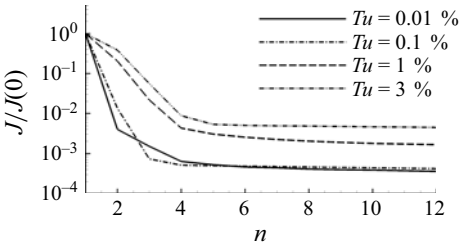

Figure 3. Convergence of the objective function J initialised by its value at the start of optimisation. Here, n is the number of optimisation iterations.

A detailed comparison of the instantaneous streamwise velocity perturbations is presented in figure 4. The left column displays the velocity perturbations in the $x-z$ plane near the wall and the right column shows the streaks at $x = 50$ in the $y-z$ plane. All plots are at the final optimisation time, i.e. $t = 100$. As the reference inflow consists solely of steady streamwise vortices, streamwise-elongated positive/negative streaks alternating in the spanwise direction are generated inside the boundary layer. In the linear regime ($Tu = 0.01\ \%$ and $Tu = 0.1\ \%$), the positive and negative streaks are almost periodically distributed. At higher Tu, the streaks exhibit greater deformation and displacement in the wall-normal direction, i.e. positive (negative) streaks approaching (leaving) the wall, a consequence of the nonlinear lift-up mechanism (Mao *et al.* 2017).

From the left column in figure 4, we observe that a close match between the reference and the predicted u' near the wall is achieved, demonstrating the effectiveness of the optimisation algorithm in capturing the critical flow characteristics that are directly linked to the wall shear stress, which is the key component in the objective function. However, the prediction accuracy degrades at higher turbulence intensity cases, as illustrated in the right column in figure 4. For $Tu = 0.01\ \%$ and $Tu = 0.1\ \%$, the reconstructed flow structures coincide with the target ones very well. The observed minor differences are primarily concentrated around the top of the streak, where the influence of the wall is less pronounced. As the turbulence intensity increases to $Tu = 1\ \%$ and $Tu = 3\ \%$, the algorithm shows improved prediction for the positive streaks. This improvement can be attributed to the flattening of the positive streaks as they are drawn towards the wall, enhancing their impact on wall shear stress, and thus contributing more significantly to the objective function. The lift-up of negative streaks can also be captured by the algorithm. However, the trapezoidal shape of the negative streaks, resulting from the nonlinear lift-up effects between the streamwise vorticity perturbation and the streaks (Mao *et al.* 2017), causes most deviations in the prediction. This discrepancy suggests that the mechanism generating the streaks might be different for the reference and reconstructed cases, which will be addressed in the following.

The reference and reconstructed inflow profiles leading to the flow development in figure 4 are shown in figure 5. The $Tu = 0.01\ \%$ case is excluded since its results are qualitatively similar to those for $Tu = 0.1\ \%$ case. As shown in the top rows of each subfigure, the reference inflow consists purely of streamwise vortices, featuring only wall-normal and spanwise velocity components. In contrast, the predicted inflow fields (bottom rows) include an additional streamwise velocity component. Despite this difference, the predicted fields retain a similar spanwise distribution to the reference inflow, but are more confined in the wall-normal direction. Specifically, the predicted inflow is concentrated in the region of $y \in [0, 1]$, which is below the flat plate wall surface ($y = 1$) downstream, and it is stretched and tilted by the curved unperturbed flow streamlines as they are advected

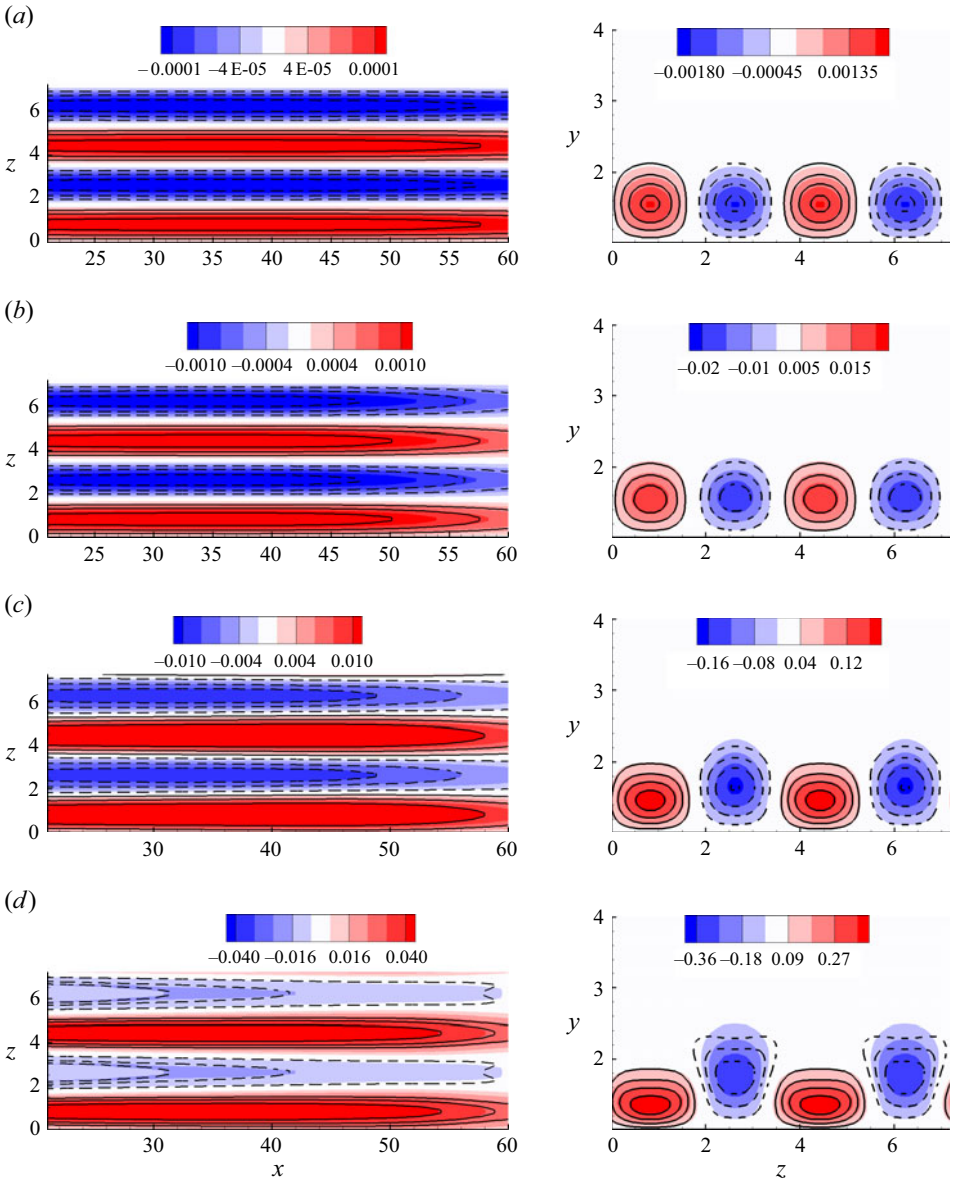

Figure 4. Comparison of the instantaneous streamwise velocity perturbation u' in the $x-z$ plane at $y=0.05$ (left column) and in the $y-z$ plane at $x=50$ (right column), for (*a*) $Tu=0.01$ %, (*b*) $Tu=0.1$ %, (*c*) $Tu=1$ % and (*d*) $Tu=3$ %. Line contours indicate the reference flow (solid: positive, dashed: negative), while colour contours represent the predicted fields.

around the leading edge (Leib *et al.* 1999). This observation indicates that the optimisation favours spatially more compact inflow structures to reproduce the stronger downstream responses associated with higher turbulence levels. Another important observation is the nonlinear scaling behaviour of the reconstructed inflows with increasing turbulence intensity. While the reference inflows are designed with consistent profiles and linearly increasing amplitude, the reconstructed inflows exhibit a nonlinear scaling behaviour with Tu.

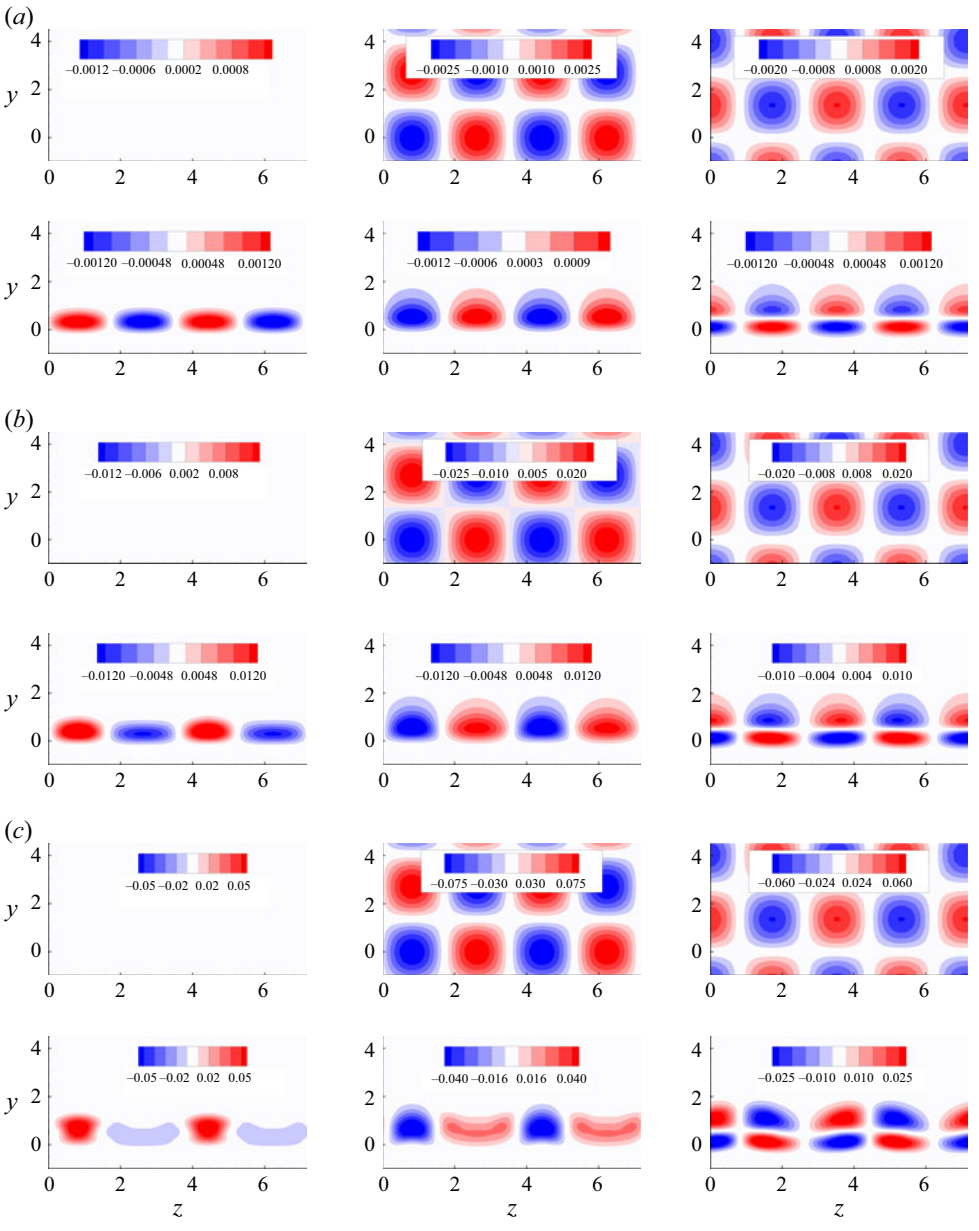

Figure 5. Comparison of the predicted and reference velocity perturbations at the inlet plane; (*a*) $Tu = 0.1\,\%$, (*b*) $Tu = 1\,\%$, (*c*) $Tu = 3\,\%$. Each row shows, from left to right, the streamwise, wall-normal and spanwise velocity perturbation, respectively. In each subfigure, the top row displays the reference velocity fields, while the bottom row shows the predicted results.

Hessian analysis is then performed for the aforementioned steady inflow cases in order to support the interpretation of the above results. As mentioned previously, a localised objective function (2.13) is adopted to quantify the influence of wall measurements on inflow perturbations at specific wall locations. To examine the effects of streamwise and spanwise variations of the wall location while maintaining computational efficiency, we construct the Hessian matrix by evaluating J_m either fixing z_m and varying x_m, or fixing

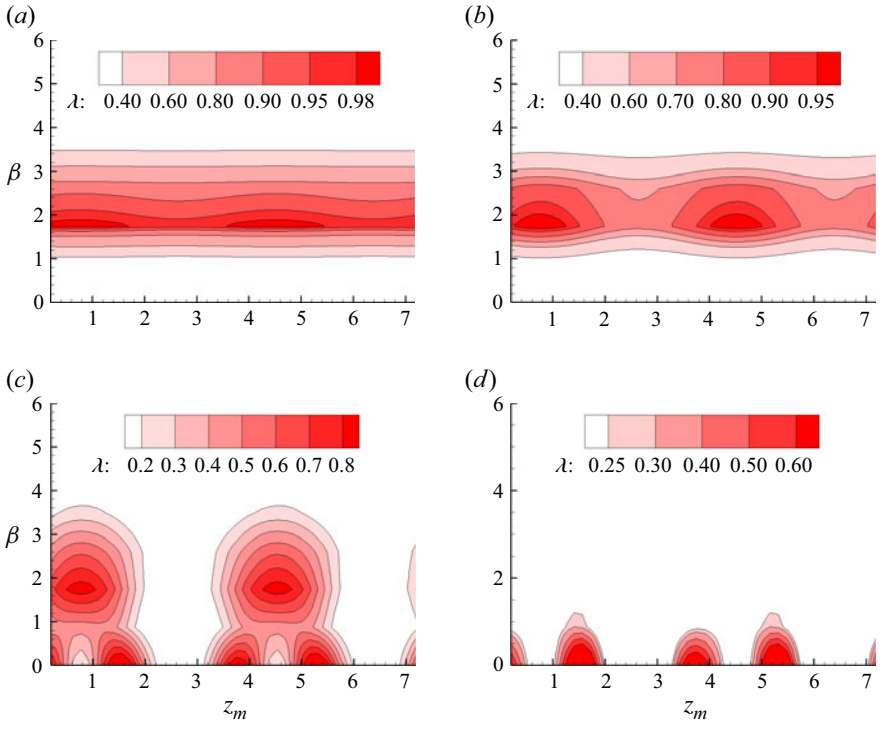

Figure 6. Contour of the largest eigenvalue of the Hessian matrix $\hat{\mathcal{H}}_z$, which is constructed by perturbing at fixed streamwise location $x_m = 48$ and across the spanwise domain; (*a*) $Tu = 0.01\,\%$, (*b*) $Tu = 0.1\,\%$, (*c*) $Tu = 1\,\%$ and (*d*) $Tu = 3\,\%$.

x_m and varying z_m, with the wall area S_m extending over the entire streamwise or spanwise direction, respectively.

We first examine the effect of spanwise measurement location on inflow observability by analysing the largest eigenvalue of the Hessian matrix $\hat{\mathcal{H}}_z$, constructed by perturbing a spanwise line at the fixed streamwise position $x_m = 48$, which approximately corresponds to the region where the downstream velocity streaks reach their peak amplitude. The resulting eigenvalue distribution is shown in figure 6. At low turbulence intensity, the eigenvalue exhibits a periodic distribution along the spanwise direction, with peaks aligned with regions of positive velocity streaks (as seen in figure 4). This suggests that inflow perturbations contributing to positive streaks are more strongly reflected in the wall response and thus more readily predicted, which is consistent with the earlier observation that positive streaks are reconstructed more accurately than negative ones. Furthermore, for the cases with $Tu = 0.01\,\%$ and $Tu = 0.1\,\%$, the dominant spanwise wavenumber is approximately $\beta = 1.8$, which aligns with the dominant spanwise wavenumber prescribed in the reference inflow. This inflow mode generates streaks of the same spanwise spacing through the lift-up mechanism, producing wall shear variations at the same wavenumber. Consequently, the wall measurement becomes most sensitive to inflow perturbations at $\beta = 1.8$, consistent with the Hessian prediction.

For $Tu = 1\,\%$, the eigenvalues associated with $\beta = 1.8$ become localised around the positive streaks, indicating that the algorithm starts to struggle with capturing the broader flow structures, i.e. the negative streaks, due to nonlinear effects. Another notable observation in figure 6(*c*) is the emergence of additional peaks located between the positive

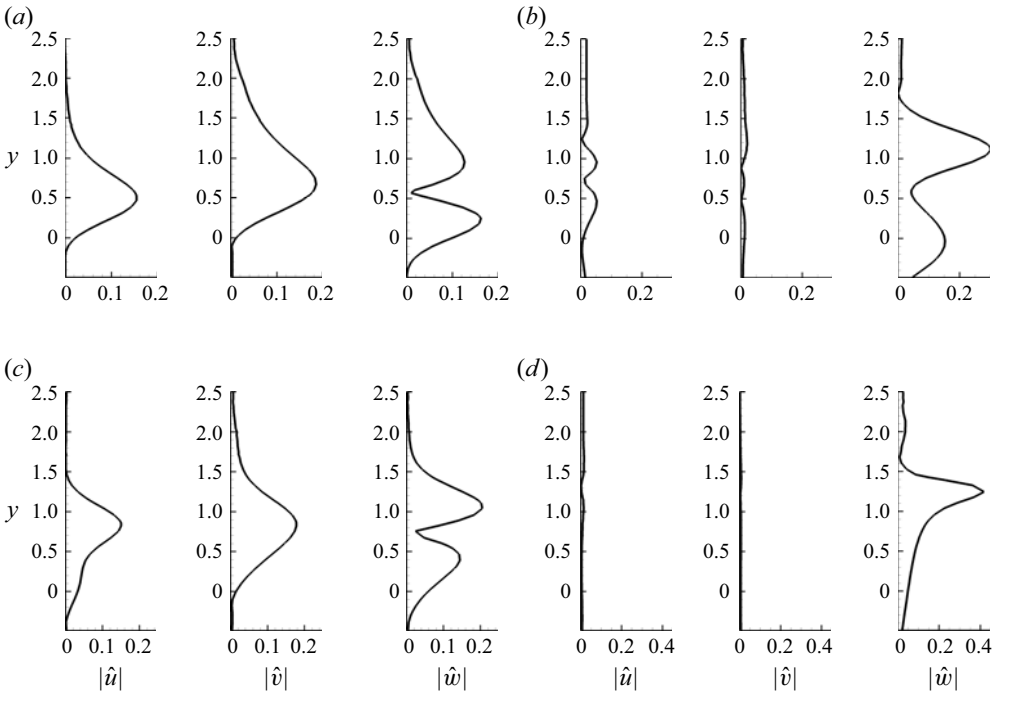

Figure 7. Visualisations of the leading eigenvectors corresponding to the eigenvalues in figure 6 at various spanwise wavenumbers: (*a*) $Tu = 0.1\ \%$, $z_m = 4.5$ and $\beta = 1.73$; (*b*) $Tu = 1\ \%$, $z_m = 3.5$ and $\beta = 0$; (*c*) $Tu = 1\ \%$, $z_m = 4.5$ and $\beta = 1.73$; (*d*) $Tu = 3\ \%$, $z_m = 3.5$ and $\beta = 0$. The first, second and third columns display the streamwise, wall-normal and spanwise component, respectively.

and negative streaks, coinciding with regions of strong spanwise shear. These peaks are associated with a 2-D mode at $\beta = 0$. The coexistence of modes at both $\beta = 1.8$ and $\beta = 0$ indicates that the wall response is influenced by multiple perturbation directions, likely due to the enhanced nonlinear interactions among inflow perturbations at higher Tu, which increase the ill conditioning of the optimisation problem. As Tu further increases, the eigenvalue spectrum becomes dominated by the $\beta = 0$ mode, which is also observed in the turbulent channel flow case in Wang & Zaki (2021). Additionally, the overall reduction in eigenvalue magnitudes with increasing Tu reflects the growing difficulty in accurately reconstructing the inflow.

Figure 7 presents selected eigenmodes corresponding to representative (β, z_m) pairs from the eigenvalue analysis in figure 6. For $Tu = 0.1\ \%$, we focus on $\beta = 1.8$ and $z_m = 4.5$, which corresponds to the location of a positive streak. The resulting eigenvector profiles are characterised by a combination of streamwise velocity perturbations and streamwise vortex pairs, similar to the predicted inflow profile as seen in figure 5. For $Tu = 1\ \%$, the eigenvector profiles associated with the two peaks in figure 6(*c*) are examined in figures 7(*b*) and 7(*c*). The eigenmode at $\beta = 1.8$ closely resembles that in the $Tu = 0.1\ \%$ case, but is shifted slightly upward in the wall-normal direction. This shift suggests that the most observable inflow perturbations become more detached from the wall with increasing Tu, possibly due to the enhanced nonlinearity. The second mode ($\beta = 0$) is dominated by the spanwise component, indicating that the observable inflow structures are in the form of spanwise perturbations. Finally, the dominant eigenmode in the $Tu = 3\ \%$ case exhibits a similar profile to the $\beta = 0$ mode at $Tu = 1\ \%$.

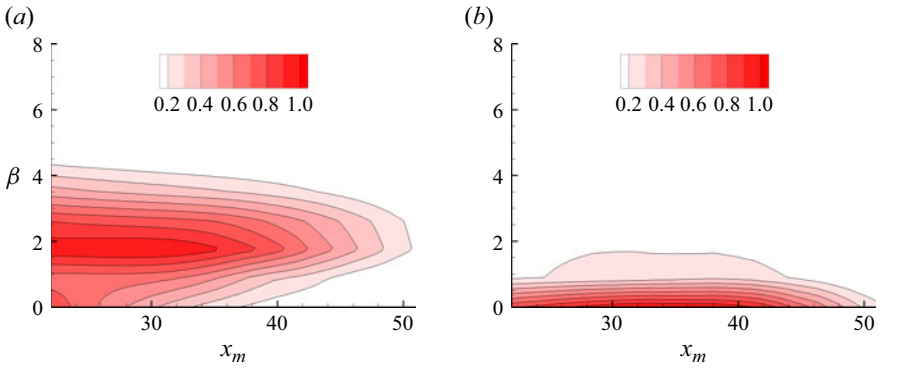

Figure 8. Contour of largest eigenvalue of the Hessian matrix, which is constructed by perturbing at fixed spanwise location z_m and across the streamwise domain; (*a*) $Tu = 0.1\,\%$ and $z_m = 4.5$, (*b*) $Tu = 3\,\%$ and $z_m = 3.6$.

Comparison with the predicted inflow in figure 5 shows that the eigenvector corresponding to $\beta = 1.8$ is clearly present in the predicted inflow. This indicates that the predicted inflow profile closely aligns with the leading eigenvector of the Hessian, meaning that the optimal solution lies along the direction in the inflow space to which the wall measurements are most responsive. Such alignment suggests improved observability and well-conditioned estimation in the low Tu cases. As Tu increases, although the predicted inflow still exhibits a dominant spanwise wavenumber around $\beta = 1.8$, the peak of the Hessian spectrum shifts to $\beta = 0$. This misalignment implies that the direction in the inflow space to which the wall measurements are most responsive no longer corresponds to the dominant inflow structure. This reflects a degradation in observability and indicates increasing ill posedness of the inverse problem.

Further inspection of the eigenvector profiles reveals distinct mechanisms of inflow observability across different turbulence levels. In the low Tu regime, the leading eigenvectors exhibit the classic streak-generating structure, characterised by streamwise velocity perturbations and streamwise vortex pairs that generate downstream streaks through the lift-up mechanism. These eigenvectors are centred at the locations of peak streak amplitude (figure 6*b*), and their high associated eigenvalues indicate strong observability at these regions. In contrast, for higher Tu, the dominant eigenvectors take the form of spanwise velocity perturbations (figure 7*d*) and are spatially located between positive and negative streaks (figure 6*d*), i.e. regions associated with strong shear. Such perturbations do not resemble streaks directly, but instead reflect large-scale modulations that influence streak formation indirectly through the tilting of wall-normal vorticity into the streamwise direction. This suggests a shift in the observable inflow structures toward more nonlinear flow generation mechanisms and a corresponding reduction in estimation robustness.

The effect of streamwise location on the wall measurement is examined by constructing the Hessian matrix with fixed z_m and varying x_m from 20 to 50. Three representative spanwise locations are selected: $z_m = 2.5$, 4.5 and 3.6, corresponding to a negative streak, a positive streak and the region between streaks, respectively. As shown in figure 8, two primary peaks emerge at $\beta = 1.8$ and $\beta = 0$, consistent with earlier observations. The eigenvalues gradually decay along the streamwise direction, suggesting that the inflow structures are less likely to be reconstructed from wall data further downstream.

The leading eigenvectors corresponding to the largest eigenvalue over all spanwise wavenumbers at each streamwise location in figures 8(*a*) and 8(*b*) are examined in

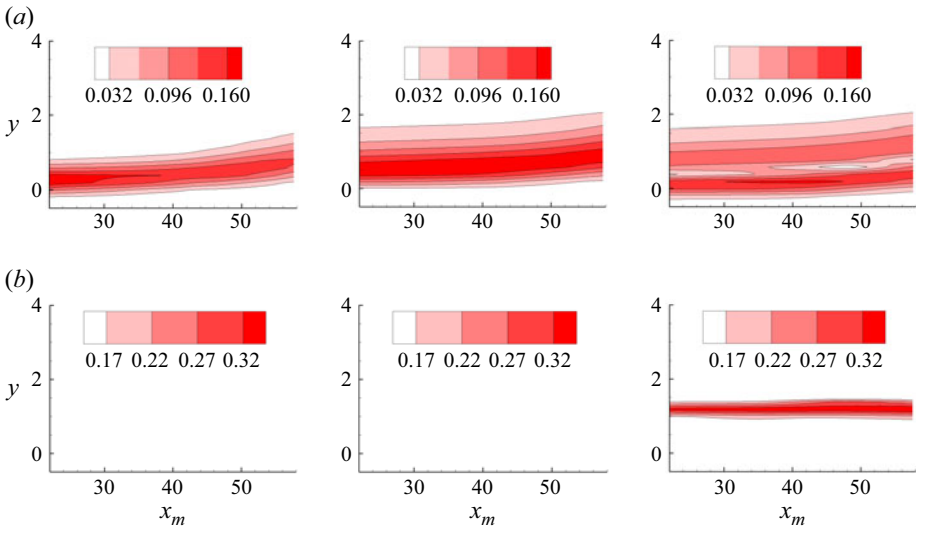

Figure 9. The leading eigenvectors corresponding to the largest eigenvalue across all spanwise wavenumbers at each streamwise location, as identified in figure 8: (*a*) $Tu = 0.1$ % and $\beta = 1.73$; (*b*) $Tu = 3$ % and $\beta = 0$. The first, second and third columns display the streamwise, wall-normal and spanwise component, respectively. Note that the first two panels in (*b*) appear empty due to the negligible magnitude of the streamwise and wall-normal components.

figures 9(*a*) and 9(*b*), respectively. These eigenmodes exhibit profiles similar to those previously discussed in figure 7. For $\beta = 1.8$, the eigenvector profiles broaden and shift upward in the wall-normal direction as x_m increases. This trend suggests that wall measurements farther downstream are more responsive to large-scale inflow perturbations that extend higher from the wall, reflecting the downstream evolution of amplified and lifted streaks within the boundary layer. For eigenmodes corresponding to $\beta = 0$, their wall-normal profiles consistently peak around $y = 1$, regardless of the observation location $\boldsymbol{x}_m$. This suggests that, for high turbulence intensity, the wall remains sensitive to the same near-wall spanwise perturbations throughout the domain. These structures are closely tied to the near-wall dynamics responsible for initiating streak formation, and their observability does not vary significantly with the streamwise measurement position.

4. Prediction of streak meandering motions

In this section, the robustness of the optimisation algorithm is evaluated by considering a more complex inflow configuration comprising multiple unsteady vortical modes (3.1). To increase the inflow complexity, 19 Fourier modes are uniformly distributed in the spanwise and wall-normal directions over the wavenumber range [0.8727, 1.65], each with a randomly assigned phase shift. In the temporal direction, 15 frequencies equally distributed in the range from 0 to 0.3665 are adopted. The turbulence intensity is set to $Tu = 1$ % and mesh 1 in table 1 is used in this section, with an optimisation time of $T = 100$.

The convergence behaviour of the cost function closely resembles that observed in the previous section and is therefore not presented for brevity. Due to the increased complexity of the inflow profile, the final reduction in J is slightly less than that observed in the single mode cases, i.e. achieving $J/J(0) < 4$ % after 20 iterations. Figure 10 provides a comparison between the reference and predicted flow by illustrating the

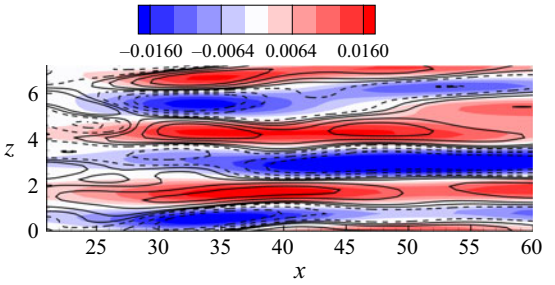

Figure 10. Instantaneous streamwise velocity perturbation u' at $y = 1.5$, $t = 100$. Colour contour represents the prediction and the line contour represents the target case with solid and dashed lines denote positive and negative values, respectively.

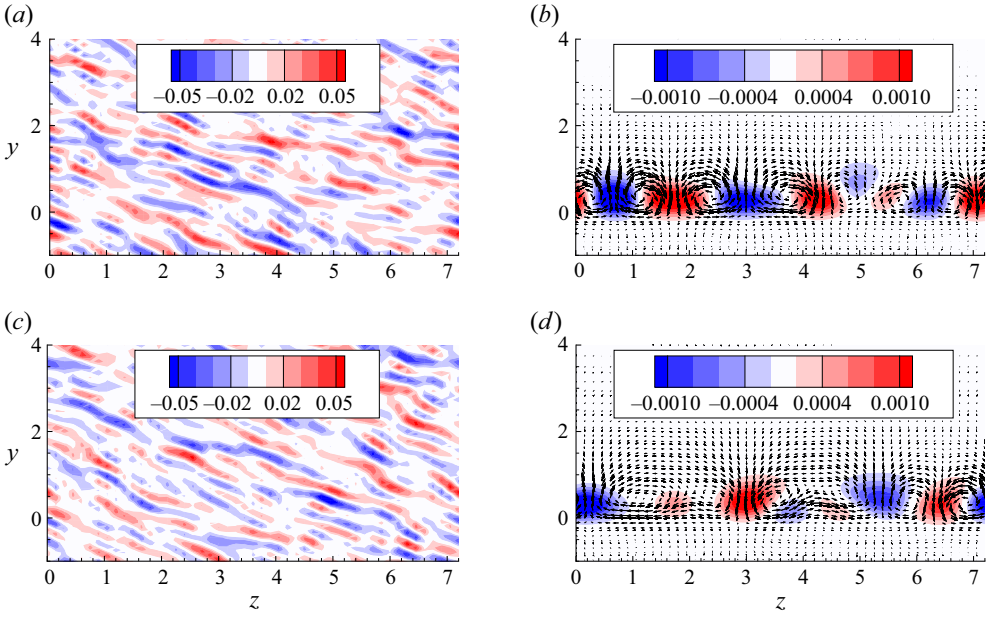

Figure 11. Comparison of real parts of the (a, c) reference and (b, d) predicted temporal inflow coefficients at (a, b) $\omega = 0.026$ and (c, d) $\omega = 0.13$. Colour contour shows the streamwise coefficient and vector field indicates the wall-normal and spanwise coefficient.

instantaneous streamwise perturbation at $t = 100$ and $y = 1.5$, where the reference flow displays complex structures characterised by pronounced streak meandering, arising from the nonlinear interaction of multiple unsteady inflow modes. Overall, the optimisation algorithm effectively reconstructs the main flow structures, demonstrating its capability to adapt to more complex inflow conditions.

Figure 11 presents a detailed comparison between the real parts of the reference and predicted inflow by showing the spatial distribution of the temporal Fourier coefficients of the inflow velocity field at two selected temporal frequencies: $\omega = 0.026$ and $\omega = 0.13$. The reference inflow, constructed from a superposition of multiple vortical modes, exhibits complex and irregular patterns, as shown in figures 11(a) and 11(c). In contrast, the reconstructed inflow has significantly lower amplitude and exhibits more organised structures, dominated by streamwise perturbations and streamwise vortices. The spanwise

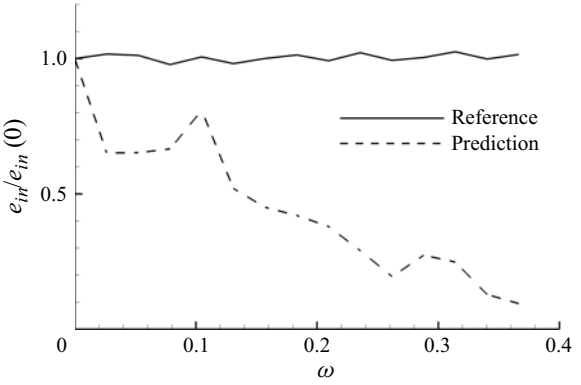

Figure 12. Energy of the Fourier coefficients of the inflow e_{in} scaled by e_{in} at $\omega = 0$ against frequency ω for $Tu = 1\,\%$.

wavenumber of these inflow structures is comparable to that observed in the forward simulations, similar to the low Tu cases discussed previously, indicating that the reconstruction successfully captures the dominant spatial scales responsible for generating downstream streaks.

The frequency content of the inflow is further analysed in figure 12, which presents the energy spectrum of the Fourier coefficients, defined as, $e_{in} = (\hat{u}_{in}^2 + \hat{v}_{in}^2 + \hat{w}_{in}^2)^{1/2}$. The value of e_{in} at $\omega = 0$ for the reference case is approximately 50 times larger than that of the reconstructed case, indicating that only a small portion of the original inflow, specifically the most wall-observable low-frequency content, is sufficient to reproduce the downstream response. To enable direct comparison of the spectral distribution between the reference and reconstructed inflows, e_{in} is normalised by its value at $\omega = 0$. In the reference case, the energy spectrum remains almost constant across all frequencies, as the Fourier amplitude is solely dependent on γ and β by definition (3.1). Conversely, the predicted case displays a clear decay in energy with increasing frequency, with a pronounced peak at $\omega = 0$. This behaviour suggests that the reconstruction is dominated by low-frequency components, which is consistent with the physical mechanism of shear sheltering (Hunt & Durbin 1999; Zaki & Saha 2009).

From figures 11 and 12, it is clear that the predicted inflow profile differs significantly from the reference, both in structure and energy distribution. This difference arises from two main reasons: first, the ill-posed nature of the current optimisation problem, where multiple inflow states can lead to similar downstream wall responses; and second, the attenuation of high-frequency inflow components by shear sheltering, which prevents them from influencing the wall measurements. It is worth noting that the main objective of this work is to explore the feasibility of reconstructing flow fields from wall measurements, with the inflow prediction serving as an intermediate step in this process. Thus, despite the differences in the predicted inflow, the results demonstrate the potential of using wall measurements to reconstruct complex flow features such as streak meandering motions.

5. Prediction of bypass transition

In this section, the robustness of the proposed framework is further evaluated using a reference inflow profile based on realistic, full-spectrum FST, enabling a boundary-layer bypass transition within the computational domain. To achieve homogeneous isotropic turbulence (HIT), an additional direct numerical simulation is conducted in a computational domain of $(l_x, l_y, l_z) = (25, 10, 36)$, with 200, 80 and 288 grid points

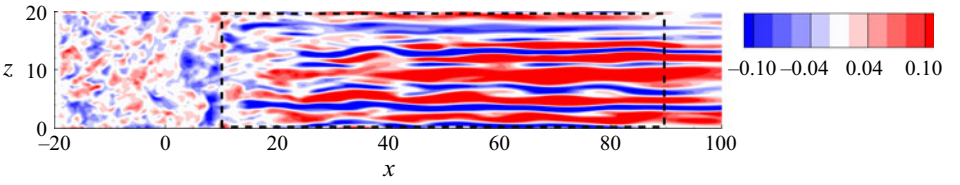

Figure 13. Contour of instantaneous streamwise velocity perturbation in the $x-z$ plane at $y = 1.5$. The box with black dashed line marks the region where wall measurements are taken.

in the streamwise, wall-normal and spanwise directions, respectively. Given the high computational demands of the optimisation procedure, the turbulence intensity is set to $Tu = 5\,\%$ with a dissipation length scale of $L_k = 2.69$. This configuration ensures that the transition is effectively triggered within the computational domain adopted in this study. The HIT inflow is then introduced as inflow perturbations at the inflow plane, positioned upstream of the leading edge at $x = -20$. Initially, mesh 2 in table (1) is employed with an optimisation time of $T = 150$, while mesh 3 is utilised for a longer optimisation time $T = 200$, as well as examining the flow development beyond the optimisation time. Figure 13 illustrates the flow development at $y = 1.5$ and $t = 150$, where streamwise-elongated positive and negative streaks with clear meandering motions are presented. The wall measurement region is marked by the dashed line.

5.1. *Prediction performance*

The current problem presents a significant reconstruction challenge, particularly under the complex FST inflow conditions, where multiple inflow configurations can produce similar wall responses, rendering it generally infeasible for the optimisation to converge to a unique global optimum. As mentioned earlier, the aim of the current work is to evaluate the capability of using wall measurements to reconstruct the corresponding flow development. Accordingly, two different initial guesses for the inflow profile are tested: $T150$, where a FST inflow is used at the start of the optimisation, and $T150_{zero}$, where a zero initial guess is adopted. In the $T150$ case, a shifted version of the reference HIT inflow (by 4 units in the wall-normal direction) is used as the initial guess. After 20 iterations, the objective function is reduced to 20 % and 5.5 % of its initial value in the $T150_{zero}$ and $T150$ cases, respectively. These reductions are less than those observed in previous inflow scenarios constructed from single or multiple vortical modes, reflecting the increased complexity of the FST inflow and the associated reconstruction challenge.

Figure 14 compares the reference inflow, shifted inflow and the optimised inflow profiles from the $T150$ and $T150_{zero}$ cases, along with their respective downstream flow fields. Among the two reconstructions, the $T150$ case yields a noticeably better agreement with the reference downstream flow, particularly in terms of streak amplitude and spatial organisation. Notably, the downstream flow generated by the shifted inflow differs significantly from the reference result, indicating that the initial guess in $T150$ does not approximate the target solution. Yet, the optimised inflow in the $T150$ case (figure 14*d*) appears visually similar to this shifted initial guess (figure 14*b*), while their resulting downstream flows differ substantially. This contrast illustrates the strong dependence of the downstream flow development to subtle variations in the inflow, a manifestation of the well-known butterfly effect in turbulent flow. Meanwhile, the downstream flow generated from the optimised inflow (figure 14*d*) closely resembles that of the reference case (figure 14*a*), indicating that the optimisation process has successfully adjusted the

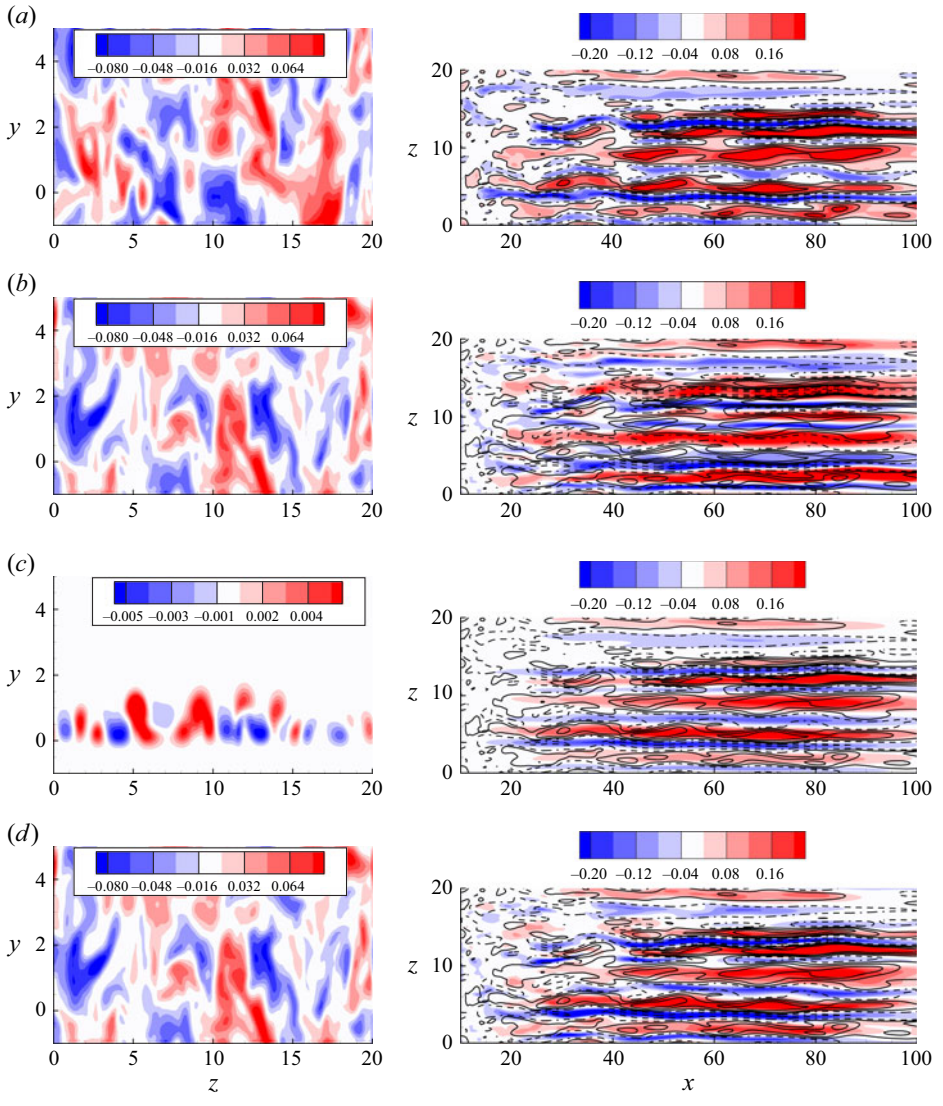

Figure 14. Instantaneous flow fields for four inflow conditions. Left column: streamwise component of inflow at $t = 0$, Right column: instantaneous streamwise velocity perturbation in the $x-z$ plane at $y = 1.5$ for (*a*) reference FST, (*b*) shifted FST, (*c*) $T150_{zero}$ and (*d*) $T150$ cases, respectively.

inflow to reproduce the correct wall response, despite inducing only small corrections to the initial condition.

The improved performance observed with the shifted inflow as the initial guess may be attributed to two factors. First, the inverse problem under consideration is inherently ill posed and nonlinear, with potentially multiple inflow configurations capable of producing similar wall responses. Consequently, different initial guesses may guide the optimisation toward distinct local minima. Second, the presence of energetic free-stream perturbations in the initial shifted inflow, although largely confined to the outer region due to shear sheltering (Zaki & Durbin 2005; Zaki 2013), may incidentally enhance the nonlinear interactions with the developing streaks beneath, thereby influencing the near-wall region and improving the agreement with the wall measurements.

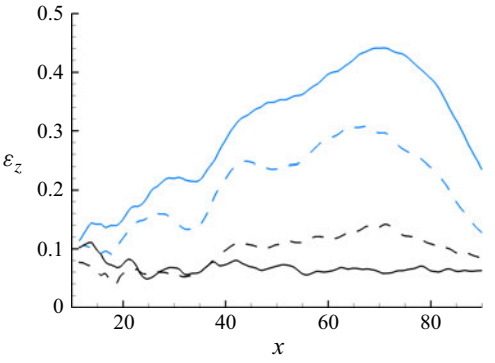

Figure 15. Streamwise variation of spanwise-averaged error ε_z between the reference and predicted $\partial u/\partial y$ at wall. Solid and dashed lines represent the $T150$ and $T150_{zero}$ cases, respectively, while blue and black lines denote results before and after optimisation, respectively.

The prediction accuracy is further quantitatively examined by the spanwise-averaged error ε_z between the reference and predicted wall data, defined as

$$\varepsilon_z = \frac{\left(\int_0^{L_z} (\mathrm{d}u_r/dy - \mathrm{d}u/\mathrm{d}y)^2 \mathrm{d}z\right)^{1/2}}{\left(\int_0^{L_z} (\mathrm{d}u/\mathrm{d}y)^2 \mathrm{d}z\right)^{1/2}}. \tag{5.1}$$

Figure 15 presents the streamwise evolution of ε_z for both the $T150_{zero}$ and $T150$ cases, including their corresponding initial guesses. Prior to optimisation, both cases exhibit considerable deviation from the reference, particularly in the $T150$ case, with a peak value reaching 45 %, indicating that the flow in this case deviates further from the reference one. After optimisation, the error in both cases is significantly reduced, but with distinct behaviours. In the $T150_{zero}$ case, ε_z increases downstream, reflecting the growing complexity and nonlinearity of the flow as streaks evolve and secondary instabilities develop. These features are more difficult to reconstruct solely from wall measurements. In contrast, the $T150$ case shows a relatively flat error profile with lower values across the domain, particularly in the downstream region.

5.2. *Effect of measurement region*

The previous section demonstrated that using the FST inflow as the initial guess results in a better flow reconstruction than the zero initial guess. The performance of the optimisation procedure also depends on the wall measurement data, as regions farther downstream capture more developed flow structures, particularly those associated with the nonlinear dynamics. In this section, the wall measurement domain is extended to $x = 140$, and the optimisation period is correspondingly increased to $T = 200$. Figure 16 shows the instantaneous streamwise velocity perturbation at $t = 200$, where the meandering motion of streaks is more pronounced than at $t = 150$ in figure 13. By this time instant, turbulent spots have already formed, as evidenced by the top panel in figure 17(*a*). The optimisation for the $T200$ case uses mesh 3 in table 1 and adopts the optimal inflow profile obtained from the $T150$ case as the initial guess. A total of 12 iterations are performed, achieving a significant reduction in the objective function by more than 60 % of its initial value.

To assess the prediction capability of the reconstructed inflow beyond the optimisation window, figure 17 presents the evolution of instantaneous wall-normal velocity fluctuation v' at four consecutive time instants from $t = 200$ to $t = 275$. The simulation beyond the optimisation period is enabled by extending the predicted inflow: the optimised inflow

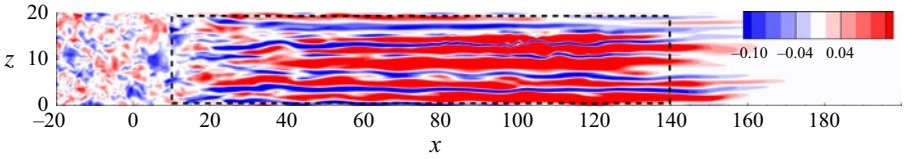

Figure 16. Contour of instantaneous streamwise velocity perturbation in the $x-z$ plane at $y = 1.5$ and $t = 200$ subject to FST. The box with black dashed line marks the region where wall measurements are recorded.

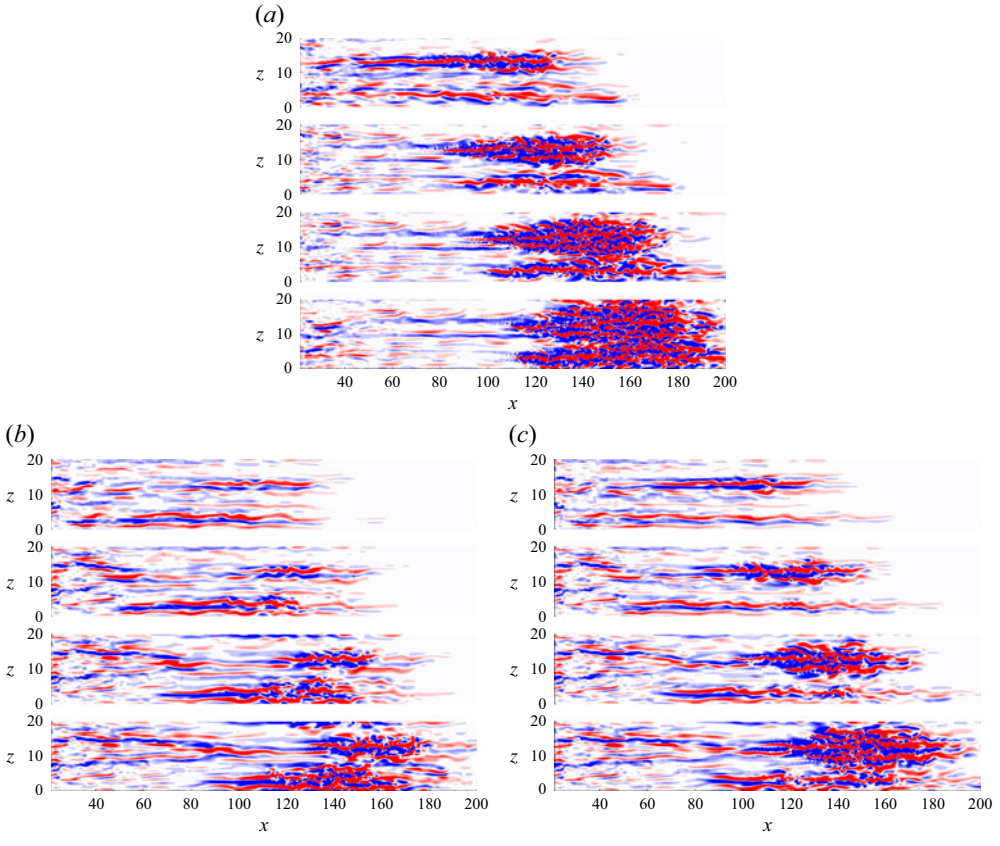

Figure 17. Contour of instantaneous wall-normal perturbation v' in the $x-z$ plane at four consecutive time instants from $t = 200$ to $t = 275$ with an increment of 25. (*a*) Reference FST case, (*b*) $T150$ case and (*c*) $T200$ case.

signal within the optimisation interval is transformed into the frequency domain via Fourier transform and then extended via inverse Fourier transform to reconstruct a longer time series. This procedure yields a periodically repeated inflow for $t > 200$, which is introduced solely to provide a continuous upstream boundary condition. Over the time interval shown, the downstream development of the turbulent spot, which is already located around $x \approx 120$ at $t = 200$, is not directly influenced by the repeated portion of the inflow imposed at the inlet ($x = -20$).

In the reference case (figure 17*a*), two dominant patches of streaks undergo secondary instability: the first breakdown occurs in the upper region around $z = 13$, followed by a second breakdown closer to $z = 5$. The $T150$ case (figure 17*b*) reproduces the emergence of turbulent spots but fails to capture the correct sequence and locations of their formation:

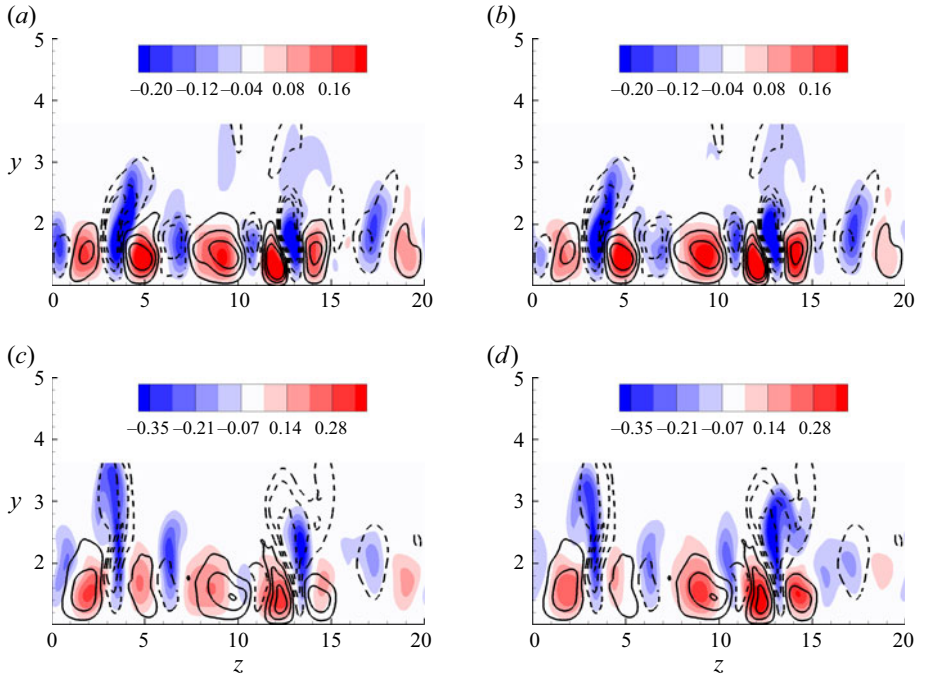

Figure 18. Instantaneous streamwise velocity perturbation u' in the $y-z$ plane at $t = 150$ and $x = 70$, (*a*) $T150$ and (*b*) $T200$; at $t = 200$ and $x = 110$, (*c*) $T150$ and (*d*) $T200$. The solid and dashed line contours represent the reference positive and negative u', respectively.

both streak patches break down approximately simultaneously and with a greater delay than observed in the reference. In contrast, the $T = 200$ case (figure 17*c*) shows notable improvement: a turbulent spot first appears near $z = 13$, consistent with the reference case, though slightly smaller in size and delayed in time. The spot grows downstream and later merges with a second spot originating near $z = 5$, similar to in the reference case.

Further insight into the influence of additional wall data is provided in figure 18, which shows the instantaneous u' in the cross-section plane at $x = 70$ ($t = 150$) and $x = 110$ ($t = 200$). At $t = 150$, both reconstructions capture the main streak structures, though with subtle differences: the $T200$ case better resolves the high-speed and low-speed streaks near $z = 13$, whereas the $T150$ result performs slightly better near $z = 5$. By $t = 200$, the $T200$ case achieves significantly closer agreement with the reference flow, especially in the upper region around $z = 13$, where streak breakdown first occurs, as previously observed in figure 17(*a*).

The improved prediction of downstream flow evolution observed in the $T200$ (figure 17*c*) can be attributed to the enhanced accuracy at $t = 200$. The inclusion of downstream wall measurements enables the optimisation process to incorporate additional spatio-temporal information associated with the early development of streak instabilities, particularly those developing near $z = 13$ that later undergo breakdown. Consequently, the predicted flow from the $T200$ case exhibits greater consistency with the reference case, not only at $t = 200$, but throughout the subsequent flow evolution, as shown in figure 17*c*.

6. Conclusions

In the present work, we demonstrate the capability of an adjoint-variational optimisation method to predict bypass transition in a boundary-layer flow over a flat plate with a

leading edge using wall measurements. By transforming the prediction problem into an optimisation one, the method seeks inflow profiles that minimise the difference between the reference and predicted streamwise velocity gradients at the wall. The optimisation algorithm is solved through a forward–backward iteration loop. Additionally, a Hessian matrix, representing the second-order derivative of the objective function with respect to the inflow, is constructed to further facilitate the interpretation of the prediction performance. The proposed approach is evaluated across three flow configurations with increasing levels of nonlinearity.

The performance of the optimisation algorithm is first evaluated by predicting steady streaks generated by pairs of streamwise vortices with various turbulence intensity levels. The algorithm accurately reconstructs the resulting velocity streaks, with particularly high accuracy in predicting positive streaks. In contrast, the prediction of negative streaks degrades as turbulence intensity increases, primarily due to their diminished influence on wall measurements. Hessian analysis reveals that the most observable inflow structures shift with increasing turbulence intensity: from classic streak-generating modes aligned with downstream streaks at low Tu, to spanwise uniform perturbations in high-shear regions at higher Tu, reflecting a transition toward more complex, nonlinearly generated flow responses.

To further assess the robustness of the proposed algorithm, a more complex inflow configuration comprising multiple vortical modes is considered. Although the reconstructed inflow differs notably from the reference in both structure and amplitude, the optimisation successfully recovers the dominant downstream flow features, with significantly reduced inflow energy. Finally, in the case of full-spectrum FST generated from a separate simulation of HIT, the algorithm reconstructs the primary streak structures. Initialising from an FST-based guess yields better accuracy than from a quiescent inflow, due to both the presence of energetic disturbances and the improved initial alignment with the reference dynamics. Additionally, extending the optimisation horizon improves the prediction of transition onset and the downstream evolution of turbulent spots.

This work demonstrates the feasibility of reconstructing boundary-layer transition flows from wall measurements using a variational optimisation framework. While the method achieves promising results across a range of inflow complexities, fundamental challenges remain due to the chaotic dynamics of turbulence and the ill-posed nature of the inverse problem. Future efforts may focus on incorporating additional types of wall measurements (e.g. pressure or spanwise shear stress), adopting receding-horizon strategies to extend the optimisation time window and incorporating prior physical knowledge (such as resolvent modes) to improve convergence, robustness and reconstruction accuracy.

Acknowledgements. The authors acknowledge the support provided by the National Natural Science Foundation of China and the National Key R&D Program of China.

Funding. This work was supported by the National Natural Science Foundation of China (Grant Nos. 12202059 and 92152109) and the National Key R&D Program of China (Grant No. 2022YFE0203700).

Declaration of interests. The authors report no conflict of interest.

References

Adrian, R. & Moin, P. 1988 Stochastic estimation of organized turbulent structure: homogeneous shear flow. *J. Fluid Mech.* **190**, 531–559.

Amaral, F.R., Cavalieri, A.V., Martini, E., Jordan, P. & Towne, A. 2021 Resolvent-based estimation of turbulent channel flow using wall measurements. *J. Fluid Mech.* **927**, A17.

BANNISTER, R.N. 2017 A review of operational methods of variational and ensemble-variational data assimilation. *Q. J. R. Meteorol. Soc.* **143**, 607–633.

BARKLEY, D., BLACKBURN, H.M. & SHERWIN, S.J. 2008 Direct optimal growth analysis for timesteppers. *Intl J. Numer. Meth. Fluids* **57**, 1435–1458.

BEWLEY, T.R., MOIN, P. & TEMAM, R. 2001 Dns-based predictive control of turbulence: an optimal benchmark for feedback algorithms. *J. Fluid Mech.* **447**, 179.

BEWLEY, T.R. & PROTAS, B. 2004 Skin friction and pressure: the 'footprints' of turbulence. *Physics D* **196**, 28–44.

CHEVALIER, M., HŒPFFNER, J., BEWLEY, T.R. & HENNINGSON, D.S. 2006 State estimation in wall-bounded flow systems. Part 2. Turbulent flows. *J. Fluid Mech.* **552**, 167–187.

COLBURN, C.H., CESSNA, J.B. & BEWLEY, T.R. 2011 State estimation in wall-bounded flow systems. Part 3. The ensemble Kalman filter. *J. Fluid Mech.* **682**, 289–303.

DU, Y., WANG, M. & ZAKI, T.A. 2023 State estimation in minimal turbulent channel flow: a comparative study of 4dvar and pinn. *Intl J. Heat Fluid Flow* **99**, 109073.

DURAISAMY, K., IACCARINO, G. & XIAO, H. 2019 Turbulence modeling in the age of data. *Annu. Rev. Fluid Mech.* **51**, 1–23.

FUKAMI, K., FUKAGATA, K. & TAIRA, K. 2019 Super-resolution reconstruction of turbulent flows with machine learning. *J. Fluid Mech.* **870**, 106–120.

HOUTEKAMER, P.L. & ZHANG, F. 2016 Review of the ensemble kalman filter for atmospheric data assimilation. *Mon. Weath. Rev.* **144**, 4489–4532.

HUNT, J.C.R. & DURBIN, P.A. 1999 Perturbed vortical layers and shear sheltering. *Fluid Dyn. Res.* **24** (6), 375.

HŒPFFNER, J., CHEVALIER, M., BEWLEY, T.R. & HENNINGSON, D.S. 2005 State estimation in wall-bounded flow systems. Part 1. Perturbed laminar flows. *J. Fluid Mech.* **534**, 263–294.

KALNAY, E., LI, H., MIYOSHI, T., YANG, S.-C. & BALLABRERA-POY, J. 2007 4d-var or ensemble Kalman filter? *Tellus* **59A**, 758–773.

KARNIADAKIS, G.E. & SHERWIN, S.J. 2005 *Spectral/HP Element Methods for Computational Fluid Dynamics*. 2nd edn. Oxford Science Publications.

LEIB, S.J., WUNDROW, D.W. & GOLDSTEIN, M.E. 1999 Effect of free-stream turbulence and other vortical disturbances on a laminar boundary layer. *J. Fluid Mech.* **380**, 169–203.

LIU, Z. & HASEGAWA, Y. 2020 Estimation of turbulent channel flow based on time-series wall measurements. *Season Kenkyu* **72**, 5–8.

MAO, X., BLACKBURN, H.M. & SHERWIN, S.J. 2013 Calculation of global optimal initial and boundary perturbations for the linearised incompressible Navier–Stokes equations. *J. Comput. Phys* **235**, 258–273.

MAO, X., BLACKBURN, H.M. & SHERWIN, S.J. 2015 Nonlinear optimal suppression of vortex shedding from a circular cylinder. *J. Fluid Mech.* **775**, 241–265.

MAO, X., ZAKI, T.A., SHERWIN, S.J. & BLACKBURN, H.M. 2017 Transition induced by linear and nonlinear perturbation growth in flow past a compressor blade. *J. Fluid Mech.* **820**, 604–632.

MARTINI, E., JORDAN, P., CAVALIERI, A.V.G., TOWNE, A. & LESSHAFFT, L. 2020 Resolvent-based optimal estimation of transitional and turbulent flows. *J. Fluid Mech.* **900**, A2.

MARXEN, O. & ZAKI, T.A. 2019 Turbulence in intermittent transitional boundary layers and in turbulence spots. *J. Fluid Mech.* **860**, 350–383.

MATSUBARA, M. & ALFREDSSON, P.H. 2001 Disturbance growth in boundary layers subjected to free-stream turbulence. *J. Fluid Mech.* **430**, 149–168.

MCKEON, B.J. & SHARMA, A.S. 2010 A critical-layer framework for turbulent pipe flow. *J. Fluid Mech.* **658**, 336–382.

MILANO, M. & KOUMOUTSAKOS, P. 2002 Neural network modeling for near wall turbulent wall. *J. Comput. Phys.* **182**, 1–26.

NOLAN, K.P. & ZAKI, T.A. 2013 Conditional sampling of transitional boundary layers in pressure gradients. *J. Fluid Mech.* **728**, 306–339.

RABIER, F. 2005 Overview of global data assimilation developments in numerical weather prediction centres. *Q. J. R. Meteorol. Soc.* **131**, 3215–3233.

RAWLINS, F., BALLARD, S.P., BOVIS, K.J., CLAYTON, A.M., LI, D., INVERARITY, G.W., LORENC, A.C. & PAYNE, T.J. 2007 The met office global four-dimensional variational data assimilation scheme. *Q. J. R. Meteorol. Soc.* **133**, 347–362.

SCHRADER, L.-U., BRANDT, L., MAVRIPLIS, C. & HENNINGSON, D.S. 2010 Receptivity to free-stream vorticity of flow past a flat plate with elliptic leading edge. *J. Fluid Mech.* **653**, 245–271.

SUZUKI, T. & HASEGAWA, Y. 2017 Estimation of turbulent channel flow at $Re_\tau = 100$ based on the wall measurement using a simple sequential approach. *J. Fluid Mech.* **830**, 760–796.

TALAGRAND, O. & COURTIER, P. 1987 Variational assimilation of meteorological observations with the adjoint vorticity equation. I: theory. *Q. J. R. Meteorol. Soc.* **113**, 1311–1328.

THACKER, W.C. 1989 The role of the hessian matrix in fitting models to measurements. *J. Geophys. Res.* **94**, 6177–6196.

TOWNE, A., LOZANO-DURAN, A. & YANG, X. 2020 Resolvent-based estimation of space-time flow statistics. *J. Fluid Mech.* **883**, A17.

WANG, Q., HASEGAWA, Y. & ZAKI, T.A. 2019*b* Spatial reconstruction of steady scalar sources from remote measurements in turbulent flow. *J. Fluid Mech.* **870**, 316–352.

WANG, B., MAO, X. & ZAKI, T.A. 2019*a* Low-frequency selectivity in flat-plate boundary layer with elliptic leading edge, *J. Fluid Mech.* **866**, 239–262.

WANG, Q., WANG, M. & ZAKI, T.A. 2022 What is observable from wall data in turbulent channel flow? *J. Fluid Mech.* **941**, A48.

WANG, M. & ZAKI, T.A. 2021 State estimation in turbulent channel flow from limited observations. *J. Fluid Mech.* **917**, A9.

WU, Z., ZAKI, T.A. & MENEVEAU, C. 2020 High-Reynolds-number fractal signature of nascent turbulence during transition. *Proc. Natl Acad. Sci.* Available at: https://www.pnas.org/content/early/2020/02/04/1916636117.full.pdf.

XIAO, D. & PAPADAKIS, G. 2017 Nonlinear optimal control of bypass transition in a boundary layer flow. *Phys. Fluids* **29**, 054103.

ZAKI, T.A. 2013 From streaks to spots and on to turbulence: exploring the dynamics of boundary layer transition. *Flow Turbul. Combust.* **91** (3), 451–473.

ZAKI, T.A. 2025 Turbulence from an observer perspective. *Annu. Rev. Fluid Mech.* **57**, 311–334.

ZAKI, T.A. & DURBIN, P.A. 2005 Mode interaction and the bypass route to transition. *J. Fluid Mech.* **531**, 85–111.

ZAKI, T.A. & SAHA, S. 2009 On shear sheltering and the structure of vortical modes in single-and two-fluid boundary layers. *J. Fluid Mech.* **626**, 111–147.

ZAKI, T.A. & WANG, M. 2021 From limited observations to the state of turbulence: fundamental difficulties of flow reconstruction. *Phys. Rev. Fluids* **6**, 100501.

ZHANG, F., ZHANG, M. & HANSEN, J.A. 2009 Coupling ensemble kalman filter with four-dimensional variational data assimilation. *Adv. Atmos. Sci.* **26**, 1–8.